

Article

Optimization of the Process Parameters of Laser Beam Powder Bed Fusion GTD222 Nickel-Based Superalloy Based on Two Laser Energy Densities

Zhiqiang Wang^{1,2}, Bo He^{1,2,*} , Zhenfeng Song^{1,2}, Liang Lan^{1,2}, Guoxin Lu³  and Shuang Gao^{1,2,*} 

- ¹ School of Material Engineering, Shanghai University of Engineering Science, Shanghai 201620, China; wzq137667667392021@163.com (Z.W.); 18895312937@163.com (Z.S.); cumtlanliang@163.com (L.L.)
- ² Research Center of High-Temperature Alloy Precision Forming, Shanghai University of Engineering Science, Shanghai 201620, China
- ³ Key Laboratory for Liquid-Solid Structural Evolution and Processing of Materials, Ministry of Education, School of Materials Science and Engineering, Shandong University, Jinan 250061, China; gxlu@sdu.edu.cn
- * Correspondence: jdhebo@163.com (B.H.); gaoshuang_alloy@163.com (S.G.)

Abstract: The effect of volume energy density and deposition energy density on the roughness, porosity, density and hardness of laser beam powder bed fusion (LBPBF) GTD222 Ni-based superalloy was systematically studied. The results showed that the roughness and porosity of the alloy decreased with the increase of the two laser energy densities, while the density and hardness increased. When the volume energy density and the deposition energy density exceeded a threshold value, the density and hardness reached the maximum value and almost remained constant. The volume energy density could be used to estimate the laser conditions for obtaining high-density LBPBF GTD222 alloy more accurately than the deposition energy density. The process parameters for the transformation of the alloy from porous to dense were determined based on the volume energy density. This study provides guidance for the optimization of the process parameters of LBPBF GTD222 alloy.

Keywords: laser beam powder bed fusion; GTD222 alloy; process parameters; volume energy density; deposition energy density



Citation: Wang, Z.; He, B.; Song, Z.; Lan, L.; Lu, G.; Gao, S. Optimization of the Process Parameters of Laser Beam Powder Bed Fusion GTD222 Nickel-Based Superalloy Based on Two Laser Energy Densities. *Metals* **2022**, *12*, 1154. <https://doi.org/10.3390/met12071154>

Academic Editor: Maciej Motyka

Received: 3 June 2022

Accepted: 6 July 2022

Published: 6 July 2022

Publisher's Note: MDPI stays neutral with regard to jurisdictional claims in published maps and institutional affiliations.



Copyright: © 2022 by the authors. Licensee MDPI, Basel, Switzerland. This article is an open access article distributed under the terms and conditions of the Creative Commons Attribution (CC BY) license (<https://creativecommons.org/licenses/by/4.0/>).

1. Introduction

The LBPBF technology is an additive manufacturing technology that can produce high-precision and complex metal parts [1–3]. It is the most promising technology in the field of metal additive manufacturing. The technology uses a focused high-energy laser beam to selectively melt a metal powder layer by layer, which then rapidly solidifies into a three-dimensional structure, that is, it can directly transform a computer-aided design model into a physical element without any mold equipment [2,4]. The LBPBF technology can be applied to a variety of alloy powders such as nickel and titanium [5,6]. The GTD222 alloy is a precipitation-strengthened Ni-based superalloy, whose matrix is γ phase solid solution, and the main strengthening phase is γ' -Ni₃(Al, Ti). The alloy shows excellent oxidation resistance and corrosion resistance and good mechanical properties at high temperature. The alloy is a key material in seawater pipelines, industrial gas turbines, aerospace and other fields [7,8]. Due to the excellent weldability of the GTD222 alloy, it has been reported that the LBPBF process could be used to fabricate the GTD222 alloy with excellent performance obtaining complex structures. In LBPBF processing in extremely hot and extremely cold conditions, some defects are prone to arise in the obtained metal parts, such as spheroidization, pores and cracks [9,10]. Therefore, the design of LBPBF process parameters is key to achieve the LBPBF fabrication of GTD222 alloy parts. The effect of the process parameters on surface roughness is one of the key points in this process. It is considered that surface roughness can be improved by optimizing the LBPBF

process parameters. Gogolewski et al., [11] showed that the surface roughness of LBPBF 316L steel increased with the increase of the rotation angle. Li et al., [12] showed that the increasing overlap rate of molten pool contributed to reducing the surface roughness of the formed parts. Khorasani et al., [13] found that the ranking of factors influencing the surface roughness of LBPBF Ti-6Al-4V alloy from the most to the least influential was as follows: heat treatment > laser power > scan pattern angle > hatch space > scan speed. The control of surface roughness is a difficult problem and challenge faced by LBPBF process. In this paper, the effects of laser power and scanning speed on the surface roughness of samples were studied.

In recent years, the research on the process parameters of the LBPBF Ni-based superalloy has gradually attracted much attention [14]. Lopez et al., [15] found that LBPBF CMSX-4 Ni-based superalloy had fewer defects than casted CMSX-4 alloy, when laser energy density was higher than 2.5 J/mm^2 . Lukina et al., [16] found that the crack of LBPBF ZhS6K-VI alloy increased with the decrease of the laser scanning speed. The LBPBF process parameters include laser power, scanning speed, scanning space and powder layer thickness [17,18]. Cao et al., [19] found that the internal morphology of Ti-6Al-4V lattices formed by the single-contour strategy in the LBPBF process largely depends on laser power and scanning speed. There is an intense interaction among these process parameters, which makes it difficult to determine the optimal LBPBF process parameters. In order to obtain optimal process parameters, laser energy density is commonly used as a measurement standard to estimate the synthetic action of these process parameters [20]. Laser energy density includes volumetric energy density [21] and deposition energy density [22]. Liverani et al., [23] studied the influence of LBPBF process parameters on the mechanical properties of 316L stainless steel based on laser energy density. It was found that the laser power determined the laser energy density and, as a result, had the greatest influence on the density of LBPBF material. Guoliang et al., [24] studied the microstructure and mechanical properties of LBPBF GTD222 Ni-based superalloy and found that the residual stress was large, leading to the generation of cracks when the laser energy density was too high. Lykov et al., [25] studied the influence of laser energy density on Cu alloy, EP648 Ni-based alloy, AlSi12 alloy and TiAl6V4 alloy and modified the formula of volumetric energy density. It was found that the modified volumetric energy density estimated more accurately the process parameters for obtaining high-density LBPBF alloys. Hann et al., [22] first proposed the formula of deposition energy density and used it to study the correlation between molten pool depth and process parameters. However, there are no reports about the optimization of the process parameters of LBPBF GTD222 alloy based on the two laser energy densities. It is important to study the effect of volume energy density and deposition energy density on the roughness, porosity density, and hardness of the alloy. The GTD222 alloy is a typical precipitation-strengthened Ni-based superalloy. Therefore, the optimization method of the process parameters in this paper is also suitable for the optimization of the LBPBF process of other similar alloys, such as IN718 alloy, CM247 alloy, IN939 alloy and IN738 alloy. The result of this study can provide a reference for researchers in the field.

2. Materials and Methods

In this experiment, GTD222 Ni-based superalloy powder was prepared by gas atomization. Its chemical composition is shown in Table 1. In the LBPBF process, the building direction is defined as the positive direction of the z-axis, the x-y plane is perpendicular to the building direction, and the x-z plane is horizontal to the building direction, as shown in Figure 1. The adopted 3D printing equipment was the HBD-80 metal rapid prototyping system from Shanghai Hanbang United 3D Tech Co., Ltd. (Shanghai, China). The technical parameters of the equipment were as follows: maximum laser power of 200 W, layer thickness of 10–40 μm and forming precision of 0.05–0.1 mm. The machine was used to fabricate various materials, including stainless, titanium alloys and Ni-based alloy powders. The laser spot size was 60 μm , the powder layer thickness was 30 μm , the laser scanning space was 80 μm . Figure 1 shows that the rotation angle between two adjacent

powder layers was 67°. Argon was used as a protective gas throughout the LBPBF process. Twenty-five cuboidal samples with a size of 10 mm × 10 mm × 10 mm were built with the HBD-80 printing equipment with an Nd:YAG laser in continuous-wave mode, as shown in Figure 2. The top surface roughness was measured with a roughness tester (Mitutoyo SJ210), and the average value of three measurements was taken as the final roughness value. The Rockwell hardness test was carried out using a Vickers HXD-1000 TMS/LCD machine with 60 kgf load and 15 s dwell time. To observe the pores, all samples were ground from 220 grit to 2000 grit and mechanically polished. Then, the polished surfaces were observed using an optical microscope (OM, Soptop ICX41M), and the porosity of the samples was calculated by Image-Pro Plus software (Image-Pro Plus6.0, Media Cybernetics, Inc., Rockville, MD, USA). In addition, the density of the samples was measured by the Archimedes drainage method.

Table 1. Chemical compositions of GTD222 alloy (wt.%).

Element	Cr	Co	W	Nb	Ta	Ti	Al	C	Zr	B	Ni
Content	22.3	18.82	1.93	0.8	0.99	2.32	1.18	0.1	0.007	0.003	Bal.

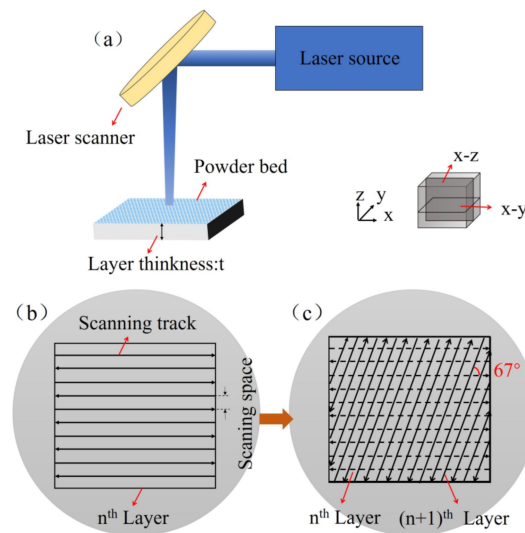


Figure 1. (a) Schematic diagram of the LBPBF process for GTD222 alloy, (b) laser scanning tracks on the *n*th layer and (c) laser scanning tracks on the *n*th layer and (*n* + 1)th layer.

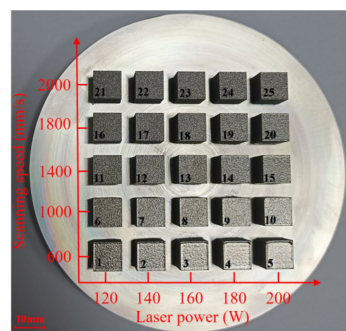


Figure 2. Appearance of 25 samples under different laser powers and scanning speeds.

In this study, the relation between the volume energy density (E_v) and the process parameters was as follows [21]:

$$E_v = \frac{P}{vSt'} \tag{1}$$

where P is the laser power, W , v is the laser scanning speed, mm/s, S is the laser scanning space, t is the powder layer thickness, E_v is the volume energy density, J/mm^3 .

The relation between the deposition energy density (E_d) and the process parameters was as follows [22]:

$$E_d = \frac{AP}{\sqrt{\pi D v \sigma^3}}, \quad (2)$$

where E_d represents the deposition energy density, D is the thermal diffusivity, A is the laser absorptivity, σ is the laser spot size. The unit of the volume energy density (E_v) is the same as that of the deposition energy density (E_d), that is, J/mm^3 . P and v are variables, but the other process parameters were constants in the present study. Thus, the main difference between Equations (1) and (2) is the index v , which contributes to E_v as v^{-1} and to E_d as $v^{-1/2}$.

3. Results

3.1. Roughness

Figure 3a shows the histogram of the top surface roughness under different laser powers and scanning speeds. It can be seen that the roughness decreased with the increase of laser power when the scanning speed was constant. Meanwhile, the roughness decreased with the decrease of scanning speed when the laser power was constant. According to Equations (1) and (2), the volumetric and deposited energy density increase with the increase of laser power or the decrease of scanning speed. This indicates that the surface quality of the as-built samples improved with the increase of laser energy density. Figure 3b,c show the change in the top surface roughness as a function of the volumetric and deposited energy density. It can be seen that the top surface roughness of the sample decreased with the increase of both volume energy density and deposition energy density. The minimum roughness value was 2.6 μm , and the maximum roughness value was 13.6 μm . In addition, the correlation coefficient R of the roughness fitted by the volume energy density was 0.983, while that of the roughness fitted by the deposition energy density was 0.942. This indicates that the volume energy density can express the change in the surface roughness of LBPBF GTD222 alloy more accurately than the deposition energy density. It can be concluded that the main factor affecting the surface roughness was the laser energy density which is determined by laser power and scanning speed. On the other hand, an excessive laser energy density will result in a very high temperature of the molten pool, which is detrimental to the dimensional accuracy of LBPBF parts. Sample No. 5 was built under the maximum laser energy density, but its top surface was hollow as shown in Figure 2. Therefore, higher quality can be obtained by controlling the laser energy density.

3.2. Porosity

Figure 4 is an OM image of the representative samples (x - y plane) under different laser energy densities. When the volume energy density was 138.0 J/mm^3 (Figure 4a) and 46.3 J/mm^3 (Figure 4b), only a few pores with small size and circular shape were found on the samples. This kind of pores were ascribed to the residual of the gas involved in molten pools. The gas could not escape in time from the molten pools due to the rapid solidification; therefore, pores with small size and round shape were generated in the sample. With the decrease of volume energy density to 25.0 J/mm^3 , the pores became larger and acquired an irregular shape (Figure 4c–e). This was attributed to the fact that the metal powder was not completely melted when the laser energy was insufficient. After the solidification of the molten pool, unmelted powder particles remained in the samples, resulting in large pores with irregular shape. This also occurred in samples with deposition energy density from 108.4 J/mm^3 to 35.6 J/mm^3 (Figure 4a–e). Figure 5a,b show the change in porosity as a function of volumetric and deposited energy density. It can be seen that the porosity decreased sharply with the increase of the two laser energy densities, when the volume energy density was less than 46.3 J/mm^3 or the deposition energy density was less than 62.5 J/mm^3 . However, when the volume energy density was greater than 46.3 J/mm^3 or the deposition energy density was more than 62.5 J/mm^3 , the porosity became almost

constant at approximately 0.005%. In addition, the correlation coefficient ($R = 0.975$) of the porosity fitted by the volume energy density was slightly larger than that ($R = 0.936$) of the porosity fitted by the deposition energy density. This also indicates that the volume energy density can indicate the change in porosity of LBPBF GTD222 alloy more accurately than the deposition energy density.

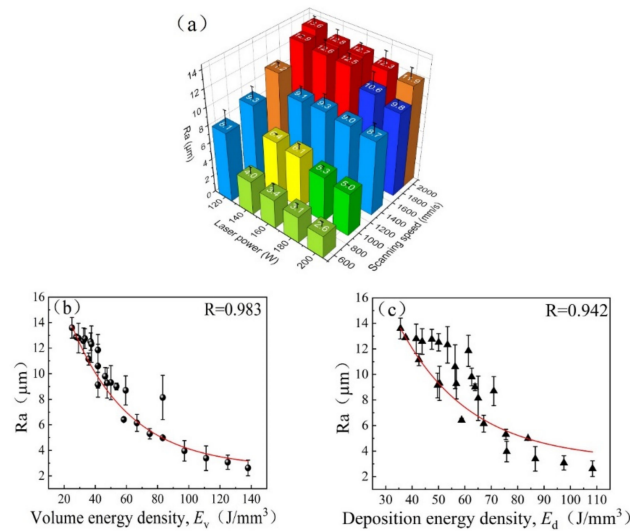


Figure 3. (a) Histogram of the top surface roughness at different laser powers and scanning speeds, showing changes in the top surface roughness as a function of (b) volume energy density and (c) deposition energy density.

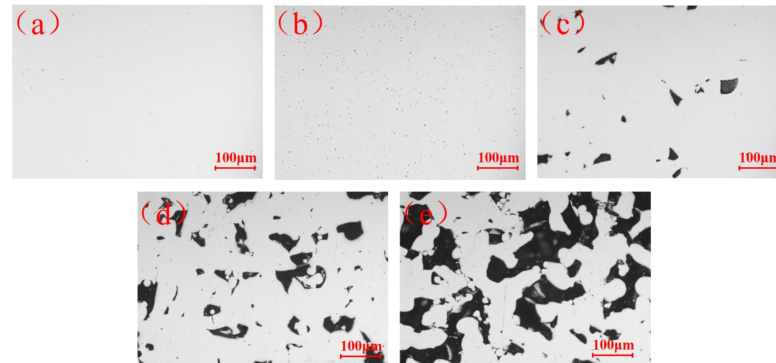


Figure 4. Optical microscope images of samples at different energy densities: (a) $E_v = 138.0 \text{ J}/\text{mm}^3$ and $E_d = 108.4 \text{ J}/\text{mm}^3$; (b) $E_v = 46.3 \text{ J}/\text{mm}^3$ and $E_d = 62.5 \text{ J}/\text{mm}^3$; (c) $E_v = 41.7 \text{ J}/\text{mm}^3$ and $E_d = 49.7 \text{ J}/\text{mm}^3$; (d) $E_v = 33.3 \text{ J}/\text{mm}^3$ and $E_d = 47.5 \text{ J}/\text{mm}^3$; (e) $E_v = 25.0 \text{ J}/\text{mm}^3$ and $E_d = 35.6 \text{ J}/\text{mm}^3$.

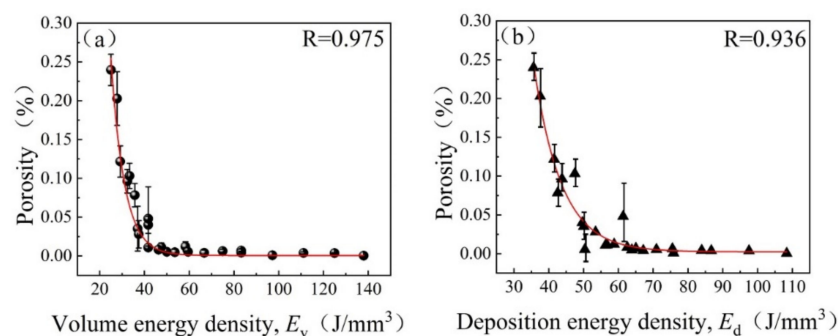


Figure 5. Change in the porosity as a function of (a) volume energy density and (b) deposition energy density.

3.3. Density

The changes in the density of LBPBF GTD222 alloy as a function of the volumetric and deposited energy density are shown in Figure 6a,b. It can be seen that the change of density involved two stages. The density increased from 6.78 to 8.29 g/mm³ when the volume energy density increased from 25.0 to 46.3 J/mm³. The density then became almost constant at approximately 8.29 g/mm³ (dense) when the volume energy density exceeded 46.3 J/mm³. In the same way, the density also increased with the increase of deposition energy density from 35.6 to 62.5 J/mm³ and became constant when the deposition energy density exceeded 62.5 J/mm³. This suggests that 46.3 J/mm³ and 62.5 J/mm³ were the threshold values of the process parameters for the alloy transformation from porous to dense. In addition, it is evident that the data points cluster on the fitting curve in Figure 6a, while they obviously deviate from the fitting curve in Figure 6b. Moreover, the correlation coefficient ($R = 0.974$) in Figure 6a is distinctly larger than that ($R = 0.872$) in Figure 6b. This shows that there is a high correlation between the volume energy density and the density of LBPBF GTD222 alloy. Therefore, the volume energy density can be used as a measure to accurately obtain the laser conditions needed to fabricate a dense LBPBF GTD222 alloy.

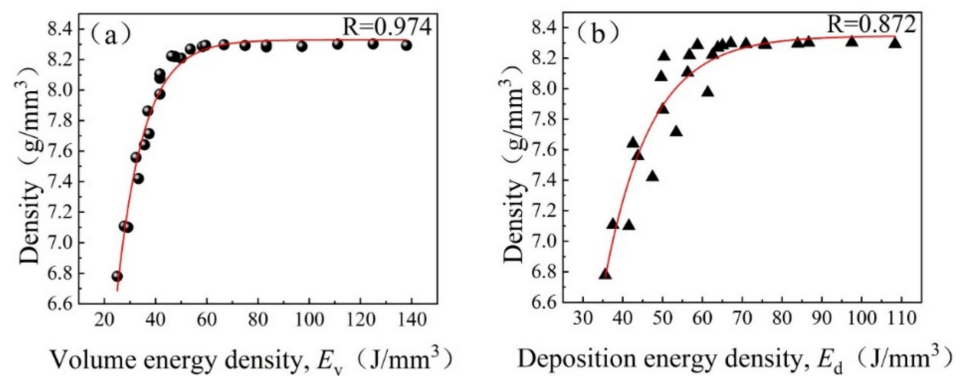


Figure 6. Change in the density of LBPBF GTD222 alloy as a function of the (a) volume energy density and (b) deposition energy density.

3.4. Hardness

Figure 7a,b show the relationship between the hardness and the two laser energy densities. Figure 7c shows the relationship between hardness and density. It can be seen in Figure 7a that the hardness of LBPBF GTD222 alloy increased from 24.3 to 54.0 HRA with the increase of the volume energy density from 25.0 to 46.3 J/mm³ (Figure 7a) or the increase of the deposition energy density from 35.6 to 62.5 J/mm³ (Figure 7b). When the volume energy density exceeded 46.3 J/mm³ or the deposition energy density exceeded 62.5 J/mm³, the hardness almost remained close to 54.0 HRA. When the volume energy density was lower than 46.3 J/mm³ or the deposition energy density was lower than 62.5 J/mm³, there was a sharp decrease in hardness. This indicates that the mechanical properties of LBPBF GTD222 alloy worsened evidently when the laser energy was not high enough. Therefore, the laser energy threshold value is also a key value for the preparation of high-hardness alloys. In addition, as shown in Figure 7c, the hardness has a clear linear relationship with the density. When the energy density was low, the powder melted incompletely, and many pores tended to form in the samples, leading to a decrease of the hardness. The powder melted relatively fully with the increase of laser energy density, contributing to the formation of a compact material with superior mechanical properties. Moreover, the correlation coefficient ($R = 0.829$) in Figure 7a is distinctly larger than that ($R = 0.700$) in Figure 7b. This also indicates that the volume energy density is more suitable to express the change in hardness of LBPBF GTD222 alloy than the deposition energy density.

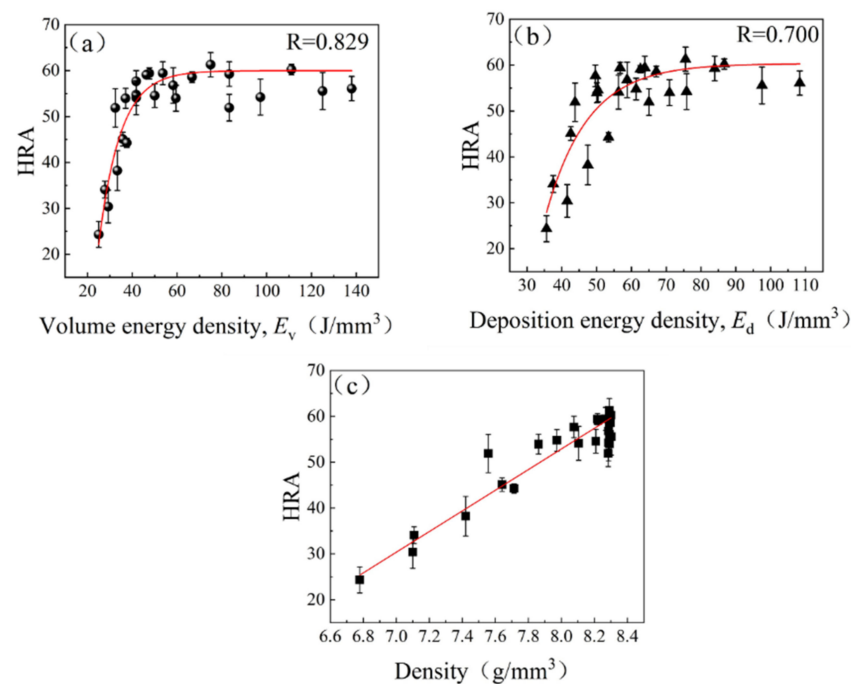


Figure 7. The hardness varies with (a) volume energy density, (b) deposition energy density and (c) density.

4. Discussion

In this study, the effects of laser energy density on the roughness, porosity, density and hardness of LBPBF GTD222 Ni-based superalloy were investigated by adjusting the laser power and scanning speed. From the above results, the volume energy density provided the threshold energy density ($46.3 J/mm^3$) at which the materials changed from porous to dense; this value was lower than the corresponding value ($62.5 J/mm^3$) of the deposition energy density. This was ascribed to the index v in Equations (1) and (2), that is, the volume energy density as v^{-1} is in Equation (1) and the deposition energy density as $v^{-1/2}$ in Equation (2). This indicated the contribution of the scanning speed was smaller than that of laser power in Equation (2). However, the contribution of the scanning speed was actually smaller than that of laser power, as proved by the above results, that is, the change in roughness, porosity, density and hardness can be indicated by one curve as a function of Equation (1), the volume energy density equation. The volume energy density has been widely used in research on LBPBF processes, and it was reported that changes in the relative density could be understood considering the value of the volume energy density [26,27]. Nevertheless, Suzuki et al., [28] considered that the relative density of LBPBF martensitic steel could be better clarified by the deposition energy density rather than the volume energy density. This suggests that the selection of laser energy density largely depends on the type of alloy, that is, the alloy's physical properties and its interaction with the laser. It was reported that the recoil pressure, sputter and Marangoni convection affect the relative density of LBPBF materials [29,30]. Therefore, the laser energy density should be carefully selected during the design and optimization of the LBPBF process parameters for different alloys. For LBPBF GTD222 alloy, the volume energy density can estimate the laser conditions to obtain a high relative density more accurately than the deposition energy density.

Figure 8 shows the forming quality of all samples with different laser powers and scanning speeds. It is shown that the volume energy density increased with the increase of laser power when the scanning speed was maintained at 600 mm/s in Figure 8. When the laser power exceeded 160 W and the corresponding volume energy density exceeded $97.2 J/mm^3$, the top surface of the sample was incomplete and hollow. Excessive laser energy is thought to lead to liquid metal splashing and burning loss, and, as a result,

the top of the samples cannot be filled completely. This seriously affects the forming quality of the samples. Therefore, the upper limit value of volume energy density is 97.2 J/mm^3 . The volume energy density for GTD222 alloy from porous to dense was proved to be 46.3 J/mm^3 in previous experiments. In addition, it can be seen in Figure 8 that all samples formed completely when the volume energy density was in the range of $46.3\text{--}97.2 \text{ J/mm}^3$. Therefore, the optimized laser energy density range was obtained for GTD222 alloy based on the volume energy density. Moreover, GTD222 alloy is a typical precipitation-strengthened Ni-base superalloy. It is deemed that the above optimization method of the process parameters is also suitable for other similar alloys, such as IN718 alloy, CM247 alloy, IN939 alloy and IN738 alloy, and thus the result of this study can provide a reference for researchers in the field.

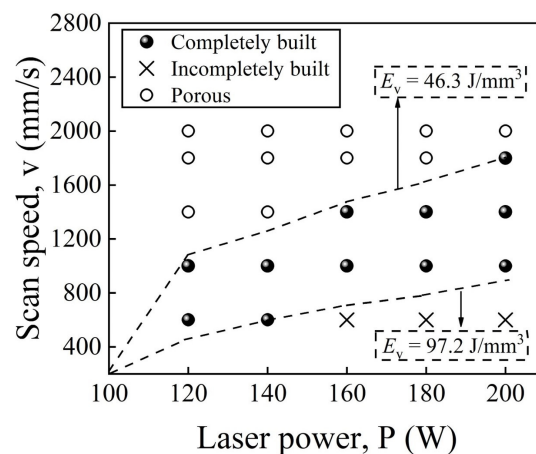


Figure 8. Forming quality of the samples under different laser conditions.

5. Conclusions

In this paper, the effect of laser energy density on the roughness, porosity, density and hardness of LBPBF GTD222 alloy were studied, and the LBPBF process parameters were optimized. The results of this research can provide a reference for the optimization of the process parameters when performing LBPBF precipitation strengthening of Ni-based superalloys. The following key conclusions can be drawn:

- (1) When the volume energy density increased from 25.0 to 46.3 J/mm^3 or the deposition energy density increased from 35.6 to 62.5 J/mm^3 , the density of LBPBF GTD222 alloy increased from 6.78 g/mm^3 to 8.29 g/mm^3 , the hardness increased from 24.3 HRA to 54.0 HRA , and the porosity decreased from 0.239 to 0.005% . When the volume energy density exceeded 46.3 J/mm^3 or the deposition energy density exceeded 62.5 J/mm^3 , the density and hardness reached the maximum value and almost remained constant.
- (2) The fitting curve between the volume energy density and the performance parameters indicates the change of the performance of LBPBF GTD222 alloy more accurately than the curve between the deposition energy density and the performance parameters. The optimized volume energy density was $46.3\text{--}97.2 \text{ J/mm}^3$.

Author Contributions: Conceptualization, S.G. and B.H.; methodology, Z.W.; software, Z.S.; validation, S.G., B.H. and G.L.; formal analysis, L.L.; investigation, Z.W.; resources, S.G.; data curation, L.L.; writing—original draft preparation, Z.W.; writing—review and editing, S.G.; visualization, G.L.; supervision, B.H.; project administration, B.H.; funding acquisition, S.G. All authors have read and agreed to the published version of the manuscript.

Funding: This research was funded by Shanghai Sailing Program (No. 19YF1417500).

Institutional Review Board Statement: Not applicable.

Informed Consent Statement: Not applicable.

Data Availability Statement: Not applicable.

Conflicts of Interest: The authors declare no conflict of interest.

References

1. Singla, A.K.; Banerjee, M.; Sharma, A.; Singh, J.; Bansal, A.; Gupta, M.K.; Khanna, N.; Shahi, A.S.; Goyal, D.K. Selective laser melting of Ti6Al4V alloy: Process parameters, defects and post-treatments. *J. Manuf. Processes* **2021**, *64*, 161–187. [[CrossRef](#)]
2. Herzog, D.; Seyda, V.; Wycisk, E.; Emmelmann, C. Additive manufacturing of metals. *Acta Mater.* **2016**, *117*, 371–392. [[CrossRef](#)]
3. Maohang, Z.; Baicheng, Z.; Yaojie, W.; Xuanhui, Q. Research progress on selective laser melting processing for nickel-based superalloy. *Int. J. Miner. Metall. Mater.* **2022**, *29*, 369.
4. Emmelmann, C.; Kranz, J.; Herzog, D.; Wycisk, E. Laser Additive Manufacturing of Metals. In *Laser Technology in Biomimetics*; Springer: Berlin/Heidelberg, Germany, 2013; pp. 143–162.
5. Yuxin, H.; Yu'e, M.; Weihong, Z.; Zhenhai, W. Effects of build direction on thermal exposure and creep performance of SLM Ti6Al4V titanium alloy. *Eng. Fail. Anal.* **2022**, *135*, 106063.
6. Zhenglei, Y.; Zezhou, X.; Yunting, G.; Renlong, X.; Ruiyao, L.; Chaorui, J.; Lunxiang, L.; Zhihui, Z.; Luquan, R. Study on properties of SLM-NiTi shape memory alloy under the same energy density. *J. Mater. Res. Technol.* **2021**, *13*, 241–250.
7. Tian, X.; Rui, W.; Zhongnan, B.; Guoliang, Z.; Qingbiao, T.; Ji, Z. Effect of Heat Treatment on Microstructure and Mechanical Properties of a Selective Laser Melting Processed Ni-Based Superalloy GTD222. *Materials* **2021**, *14*, 3668.
8. Rui, W.; Guoliang, Z.; Qingbiao, T.; Wenzhe, Z.; Chao, Y.; Donghong, W.; Anping, D.; Da, S.; Liang, Z.; Baode, Z. Effect of high temperature aging on microstructures and tensile properties of a selective laser melted GTD222 superalloy. *J. Alloy. Compd.* **2021**, *853*, 157226.
9. Sadowski, M.; Ladani, L.; Brindley, W.; Romano, J. Optimizing quality of additively manufactured Inconel 718 using powder bed laser melting process. *Addit. Manuf.* **2016**, *11*, 60–70. [[CrossRef](#)]
10. Zhijun, T.; Shuang, G.; Liang, L.; Bo, H. Effect of Rescanning Strategy on Residual Stress and Distortion of Two Alloys Manufactured by Selective Laser Melting. *J. Mater. Eng. Perform.* **2021**, *30*, 6493–6501.
11. Gogolewski, D.; Bartkowiak, T.; Kozior, T.; Zmarzly, P. Multiscale Analysis of Surface Texture Quality of Models Manufactured by Laser Powder-Bed Fusion Technology and Machining from 316L Steel. *Materials* **2021**, *14*, 2794. [[CrossRef](#)]
12. Li, C.; White, R.; Fang, X.Y.; Weaver, M.; Guo, Y.B. Microstructure evolution characteristics of Inconel 625 alloy from selective laser melting to heat treatment. *Mater. Sci. Eng. A* **2017**, *705*, 20–31. [[CrossRef](#)]
13. Khorasani, A.M.; Gibson, I.; Ghasemi, A.; Ghaderi, A. Modelling of laser powder bed fusion process and analysing the effective parameters on surface characteristics of Ti-6Al-4V. *Int. J. Mech. Sci.* **2020**, *168*, 105299. [[CrossRef](#)]
14. Nguyen, Q.B.; Luu, D.N.; Nai, S.M.L.; Zhu, Z.; Chen, Z.; Wei, J. The role of powder layer thickness on the quality of SLM printed parts. *Arch. Civil. Mech. Eng.* **2018**, *18*, 948–955. [[CrossRef](#)]
15. Lopez-Galilea, I.; Rutttert, B.; He, J.; Hammerschmidt, T.; Drautz, R.; Gault, B.; Theisen, W. Additive manufacturing of CMSX-4 Ni-base superalloy by selective laser melting: Influence of processing parameters and heat treatment. *Addit. Manuf.* **2019**, *30*, 100874. [[CrossRef](#)]
16. Lukina, E.A.; Bazaleeva, K.O.; Petrushin, N.V.; Treninkov, I.A.; Tsvetkova, E.V. Effect of the selective laser melting parameters on the structure–phase state of a ZhS6K-VI nickel superalloy. *Russ. Metall.* **2017**, *2017*, 594–600. [[CrossRef](#)]
17. Shuang, G.; Zhijun, T.; Liang, L.; Bo, H. Effects of geometrical size and structural feature on the shape-distortion behavior of hollow Ti-alloy blade fabricated by additive manufacturing process. *J. Laser Appl.* **2020**, *32*, 032005.
18. Prashanth, K.G.; Scudino, S.; Maity, T.; Das, J.; Eckert, J. Is the energy density a reliable parameter for materials synthesis by selective laser melting? *Mater. Res. Lett.* **2017**, *5*, 386–390. [[CrossRef](#)]
19. Cao, X.; Carter, L.N.; Villapún, V.M.; Cantaboni, F.; De Sio, G.; Lowther, M.; Louth, S.E.T.; Grover, L.; Ginestra, P.; Cox, S.C. Optimisation of single contour strategy in selective laser melting of Ti-6Al-4V lattices. *Rapid Prototyp. J.* **2022**, *28*, 907–915. [[CrossRef](#)]
20. Scipioni Bertoli, U.; Wolfer, A.J.; Matthews, M.J.; Delplanque, J.-P.R.; Schoenung, J.M. On the limitations of Volumetric Energy Density as a design parameter for Selective Laser Melting. *Mater. Design* **2017**, *113*, 331–340. [[CrossRef](#)]
21. Pal, S.; Lojen, G.; Kokol, V.; Drstvensek, I. Evolution of metallurgical properties of Ti-6Al-4V alloy fabricated in different energy densities in the Selective Laser Melting technique. *J. Manuf. Processes* **2018**, *35*, 538–546. [[CrossRef](#)]
22. Hann, D.B.; Iammi, J.; Folkes, J. A simple methodology for predicting laser-weld properties from material and laser parameters. *J. Phys. D Appl. Phys.* **2011**, *44*, 445401. [[CrossRef](#)]
23. Liverani, E.; Toschi, S.; Ceschini, L.; Fortunato, A. Effect of selective laser melting (SLM) process parameters on microstructure and mechanical properties of 316L austenitic stainless steel. *J. Mater. Processing Technol.* **2017**, *249*, 255–263. [[CrossRef](#)]
24. Guoliang, Z.; Weitao, P.; Rui, W.; Donghong, W.; Da, S.; Liang, Z.; Anping, D.; Baode, S. Microstructures and mechanical properties of GTD222 superalloy fabricated by selective laser melting. *Mater. Sci. Eng. A* **2021**, *807*, 140668.
25. Lykov, P.A. The Energy Density as a Reliable Parameter for Characterization of Selective Laser Melting of Various Alloys. *Mater. Sci. Forum* **2019**, *946*, 972–977. [[CrossRef](#)]
26. Kempen, K.; Yasa, E.; Thijs, L.; Kruth, J.P.; Van Humbeeck, J. Microstructure and mechanical properties of Selective Laser Melted 18Ni-300 steel. *Phys. Procedia* **2011**, *12*, 255–263. [[CrossRef](#)]

27. Casalino, G.; Campanelli, S.L.; Contuzzi, N.; Ludovico, A.D. Experimental investigation and statistical optimisation of the selective laser melting process of a maraging steel. *Opt. Laser Technol.* **2015**, *65*, 151–158. [[CrossRef](#)]
28. Suzuki, A.; Nishida, R.; Takata, N.; Kobashi, M.; Kato, M. Design of laser parameters for selectively laser melted maraging steel based on deposited energy density. *Addit. Manuf.* **2019**, *28*, 160–168. [[CrossRef](#)]
29. Qiu, C.; Panwisawas, C.; Ward, M.; Basoalto, H.C.; Brooks, J.W.; Attallah, M.M. On the role of melt flow into the surface structure and porosity development during selective laser melting. *Acta Mater.* **2015**, *96*, 72–79. [[CrossRef](#)]
30. Khairallah, S.A.; Anderson, A.T.; Rubenchik, A.; King, W.E. Laser powder-bed fusion additive manufacturing: Physics of complex melt flow and formation mechanisms of pores, spatter, and denudation zones. *Acta Mater.* **2016**, *108*, 36–45. [[CrossRef](#)]